ACS APPLIED MATERIALS & INTERFACES

www.acsami.org

Research Article

# Wearable Sensor Patch with Hydrogel Microneedles for In Situ Analysis of Interstitial Fluid

Yumin Dai,[▽] James Nolan,[▽] Emilee Madsen,[▽] Marco Fratus,[▽] Junsang Lee, Jinyuan Zhang, Jongcheon Lim, Seokkyoon Hong, Muhammad A. Alam,* Jacqueline C. Linnes,* Hyowon Lee,* and Chi Hwan Lee*

Cite This: https://doi.org/10.1021/acsami.3c12740

Read Online

ACCESS | Metrics & More | Article Recommendations | Supporting Information

**ABSTRACT:** Continuous real-time monitoring of biomarkers in interstitial fluid is essential for tracking metabolic changes and facilitating the early detection and management of chronic diseases such as diabetes. However, developing minimally invasive sensors for the in situ analysis of interstitial fluid and addressing signal delays remain a challenge. Here, we introduce a wearable sensor patch incorporating hydrogel microneedles for rapid, minimally invasive collection of interstitial fluid from the skin while simultaneously measuring biomarker levels in situ. The sensor patch is stretchable to accommodate the swelling of the hydrogel microneedles upon extracting interstitial fluid and adapts to skin deformation during measurements, ensuring consistent sensing performance in detecting model biomarker concentrations, such as glucose and lactate, in a mouse model. The sensor patch exhibits in vitro sensitivities of 0.024 ± 0.002 $\mu$A mM$^{-1}$ for glucose and 0.0030 ± 0.0004 $\mu$A mM$^{-1}$ for lactate, with corresponding linear ranges of 0.1−3 and 0.1−12 mM, respectively. For in vivo glucose sensing, the sensor patch demonstrates a sensitivity of 0.020 ± 0.001 $\mu$A mM$^{-1}$ and a detection range of 1−8 mM. By integrating a predictive model, the sensor patch can analyze and compensate for signal delays, improving calibration reliability and providing guidance for potential optimization in sensing performance. The sensor patch is expected to serve as a minimally invasive platform for the in situ analysis of multiple biomarkers in interstitial fluid, offering a promising solution for continuous health monitoring and disease management.

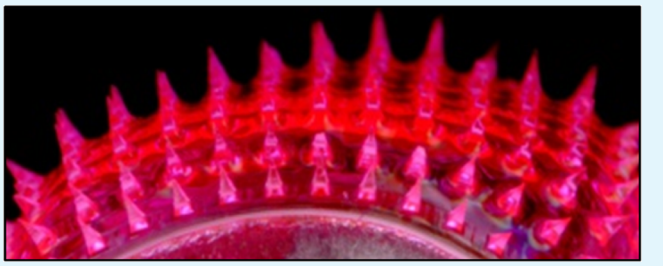

**KEYWORDS:** *interstitial fluid analysis, wearable sensor patch, hydrogel microneedles, continuous health monitoring, biomarker detection*



## INTRODUCTION

Interstitial fluid (ISF) is a biofluid that originates from transcapillary blood exchange, and its potential for in situ biomarker analysis has gained considerable interest.[1−4] It shares at least 84% of key biomarkers with plasma, including glucose and lactate, demonstrating a strong correlation between the levels of these biomarkers in ISF and blood.[5,6] The in situ analysis of ISF enables the real-time tracking of metabolic changes within tissues, thereby facilitating early detection of diseases and paving the way for personalized medical interventions. Given its direct interaction with relevant cells and tissues, ISF allows the measurement of multiple biomarkers that are either unique to it or found in higher concentrations than in conventional blood or urine tests.[7,8] Drawing ISF from the subdermis and analyzing its biomarkers on-site can overcome various obstacles, including potential contamination from skin residues and the surrounding environment, as well as the naturally low production rate of biofluids, such as sweat, from the skin.[9,10]

Wearable in situ sensing platforms have emerged, offering potential for real-time biomarker monitoring by extracting ISF through either ionophoresis or sonophoresis.[11] Ionophoresis methods use skin-mounted electrodes to generate an electrical charge, inducing the movement of charged particles within ISF and facilitating neutral particle transport, such as glucose, for sampling and measurement.[12] Sonophoresis methods apply low-frequency ultrasound to increase skin porosity through cavitation bubble induction, followed by vacuum pressure application to extract ISF for analysis.[13] The noninvasive nature of these approaches offers valuable advantages in patient comfort and ease of use, but they encounter challenges such as potential interference with biomarkers from sweat, along with possible skin irritation.[14] Additionally, existing devices face limitations in predicting and compensating for measurement delays, affecting the accuracy and effectiveness of real-time monitoring.[15]

Received: August 26, 2023
Accepted: October 7, 2023

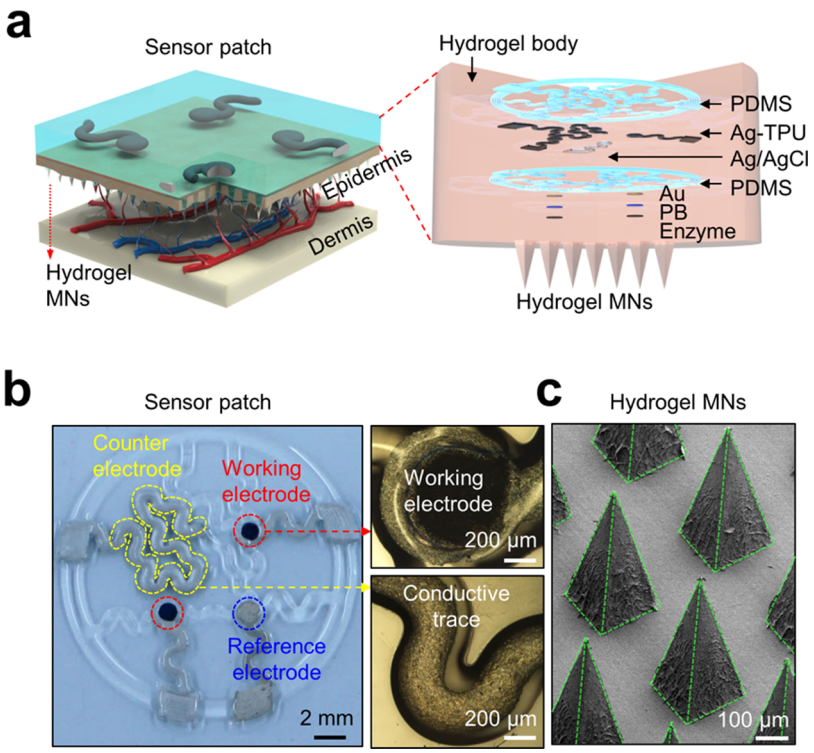


**Figure 1.** Schematics and images of the sensor patch. (a) Schematic representation showing the sensor patch applied to the skin (left), with an exploded view revealing the unassembled components of the sensor patch (right). (b) Photograph illustrating the fully constructed sensor patch without MNs, accompanied by zoomed-in microscope images of the working electrode and the conductive trace. (c) Image captured under SEM displaying the hydrogel MNs.

Microneedles (MNs), which come in a variety of materials and structures, offer a way to extract ISF in a minimally invasive manner by piercing the skin.[16−20] However, hollow MNs face challenges, such as fracturing, complex manufacturing, empirical/iterative design, limited flexibility and durability, or brittleness.[21−23] Hydrogel-based MNs constructed from materials such as poly(vinyl alcohol) (PVA), chitosan, osmolytes, and methacrylated hyaluronic acid (MeHA) have demonstrated their efficacy in ISF extraction, attributed to their rapid fluid extraction rates, biosafety, and streamlined synthesis procedure.[24−27] Yet, integrating these hydrogel MNs with sensing modules remains challenging because of mechanical mismatches or complications arising from hydrogel swelling upon absorbing ISF.[28] As a result, ISF is often collected using MNs and subsequently extracted and then analyzed using specialized lab equipment, facing issues such as sampling variability, time lags, sample degradation, and contamination, ultimately diminishing measurement accuracy and convenience.[29−31] This highlights the need for in situ ISF analysis to provide real-time data on multiple target biomarkers, thus improving both accuracy and user acceptance.

Here, we introduce a wearable sensor patch incorporating hydrogel MNs for rapid, minimally invasive collection of ISF from the skin while simultaneously measuring biomarker levels in situ. The hydrogel MNs, composed of MeHA, are designed with specific compositions and sizes to accelerate ISF extraction rates, minimize tissue invasiveness, and achieve an ideal swelling ratio. The sensor patch is designed to seamlessly integrate with the MNs, allowing its stretchability to effectively accommodate the swelling of the hydrogel during ISF extraction and to adapt to changes in skin deformation throughout the measurements. The sensor patch features a three-electrode system with glucose oxidase (GOx) and lactate oxidase (LOx) deposited on Prussian Blue (PB)-modified printed electrodes.

This setup enables reliable detection of glucose and lactate as prototype biomarkers, showing in vitro sensitivities of 0.024 ± 0.002 and 0.0030 ± 0.0004 $\mu$A mM$^{-1}$, respectively, and linear ranges of 0.1−3 and 0.1−12 mM in a bath solution. Studies conducted in vivo using a mouse model have demonstrated its capacity to continuously monitor glucose levels in real time over several hours following intraperitoneal injections of insulin or glucose. The in vivo sensitivity and detection range were gauged at 0.020 ± 0.001 $\mu$A mM$^{-1}$ and 1−8 mM, respectively. These findings correspond with those from in vitro evaluations and are consistent with results reported for devices featuring MNs.[32,33] The signal response to lactate exhibits peak-response patterns subsequent to subcutaneous lactate injections, a phenomenon that can be attributed to the unique metabolic pathway. When lactate is injected subcutaneously, it disperses into the bloodstream and is then transported to specific organs, notably the liver, for metabolic processing and utilization. This pattern aligns with previous findings.[34] Predictive modeling and simulation of the sensor patch suggests a response signal delay time of less than 10 min for glucose and lactate. These outcomes indicate superior performance compared to the typical measurement delay of 20−35 min observed with pre-extracted ISF or blood samples and the 10−20 min delay associated with previously reported devices featuring with MNs.[22,35,36] This study establishes the foundation for continuous, on-site, real-time sensing of multiple biomarkers in ISF using conformal MN patches and introduces a model to counter signal delays.


https://doi.org/10.1021/acsami.3c12740
ACS Appl. Mater. Interfaces XXXX, XXX, XXX−XXX

## RESULTS AND DISCUSSION

**Device Configuration and Working Principle.** Figure 1a depicts a comprehensive diagram of the sensor patch, showcased both in its unassembled form and when applied to skin. Primarily, the sensor patch comprises a substrate and encapsulation, both fashioned from polydimethylsiloxane (PDMS), in addition to a conductive layer constructed from thermoplastic polyurethane (TPU) embedded with either silver flakes (Ag-TPU) or silver/silver chloride (Ag/AgCl). The Ag-TPU performs dual functions as the working and counter electrodes with the Ag/AgCl serving as the reference electrode, creating a robust three-electrode system. The counter electrodes have a larger area than the working electrodes, which ensures signal stability.[37] Subsequently, Au was electroplated onto the working electrodes. This process was succeeded by the application of a PB transducer layer by using cyclic voltammetry. The enzyme layer, consisting of either GOx or LOx, was then attached to the working electrodes. Concurrently, MeHA was used to fabricate both the hydrogel body and MNs. Details of fabricating the sensor patch are described in the Methods section.

Figure 1b presents visuals of the fully constructed sensor patch. The design features circular working and reference electrodes to maximize surface area, and a serpentine-shaped counter electrode.[38] For easy wiring connectivity to the MultiPalmSens4 potentiostat (PalmSens, BASi, Inc., Houten, Netherlands) used for signal measurement, the electrodes were linked to a quasi-rectangular pad through serpentine conductive traces. Figure 1c provides the scanning electron microscope (SEM) image of the hydrogel MNs, arranged in a 15 × 15 array, with each MN having a square pyramidal shape, a length of 600 $\mu$m, a base width of 300 $\mu$m, and a tip-to-tip distance of 500 $\mu$m. Figure S1 provides optical microscope images of the sensor patch, highlighting the hydrogel MNs on the surface.

**Mechanical Characterization.** Figure 2a schematically depicts the stretched sensor patch during ISF extraction, illustrating the swelling of both the hydrogel body and the MNs upon ISF extraction. Figure 2b (black line) displays the experimental results of the swelling ratio using three sensor patches inserted into an agarose gel covered with Parafilm M, simulating the skin.[39] The dimensions of the hydrogel MNs were measured every 5 min, revealing a saturation point at approximately 9% swelling. The swelling ratio was defined as $\Delta P/P$, where $\Delta P$ represents the difference between the current and initial perimeters and $P$ is the initial perimeter value. Figure 2b (red line) illustrates the estimated maximum principal strains (<15%) experienced by the conductive layer of the sensor patch without MN over time. The corresponding results from Finite Element Analysis (FEA) are shown in Figure S2a. The swelling ratio data were fitted to an exponential model.[40]

$$\mathrm{SR} = a(1 - \mathrm{e}^{-bt}) \quad (1)$$

where SR is the swelling ratio, $a$ and $b$ are the constants for fitting, and $t$ is the swelling time. Without MNs, the sensor patch has a Young's modulus of 140 kPa, making it nearly 120 times softer than the hydrogel body and MNs under uniaxial stress along the direction of the reference electrode trace (Figure S2b). This characteristic ensures that the electrical circuit of the sensor patch remains both stretchable and robust during hydrogel swelling.

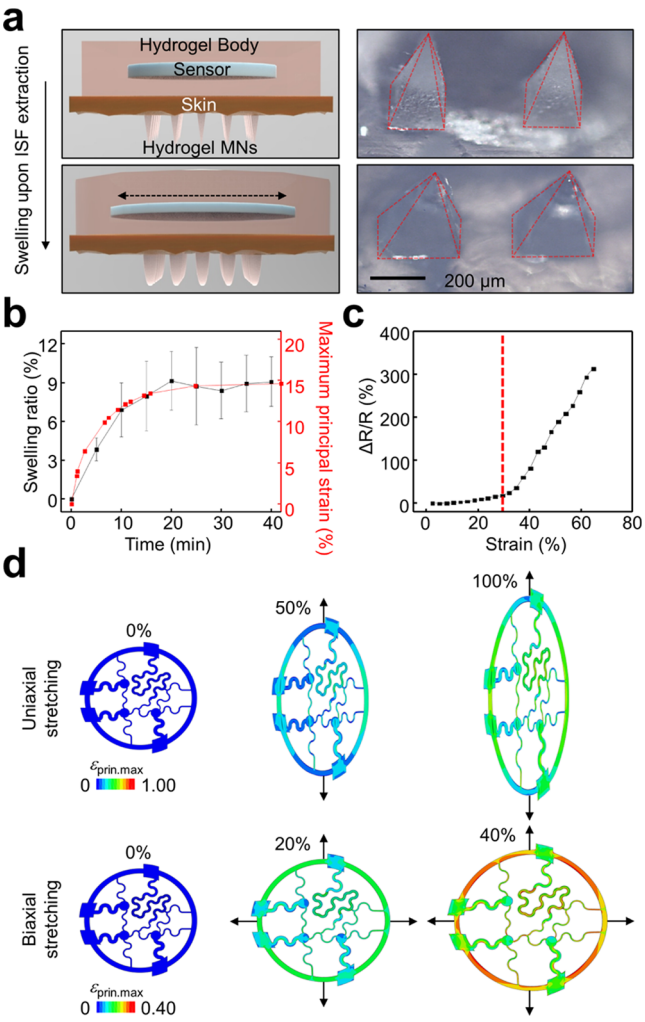


**Figure 2.** Mechanical characterization. (a) Schematic of the sensor patch during ISF extraction (left) and the corresponding optical images of hydrogel MNs (right). (b) Swelling ratio (black) and estimated maximum principal strain (red) of the sensor patch over time in swelling test ($n$ = 3). (c) Relative resistance change of the sensor patch in response to strain. (d) FEA results of the sensor patch under uniaxial or biaxial stretching.

The sensor patch without MNs exhibited an insignificant relative resistance change ($\Delta R/R$ < 20%) when subjected to strains below 30% (Figure 2c). However, at higher strains, $\Delta R/R$ increased rapidly as the serpentine traces straightened. To further assess the stability of the sensor patch without MNs, cyclic tests were conducted for 1000 cycles under 10, 15, and 20% strain, revealing that the $\Delta R/R$ remained below 10, 20, and 50%, taking into account the sensor arrays saturated swelling ratio of approximately 10% (Figure S2c). The FEA results in Figure 2d validate that the conductive layer experienced a maximum principal strain of 74% under uniaxial stretching up to 100 and 38% under biaxial stretching up to 40%, respectively. Additionally, under 30% uniaxial or biaxial stretching, the conductive layer would experience a maximum principal strain of 28 or 30%. This is greater than the maximum principal strain obtained from the swelling test, demonstrating the stable generation of electrical signals from the sensor patch during measurements. In the biaxially stretched state, a relatively greater strain concentration was observed compared to uniaxial stretching, leading to fractures occurring at 40%


https://doi.org/10.1021/acsami.3c12740
ACS Appl. Mater. Interfaces XXXX, XXX, XXX−XXX

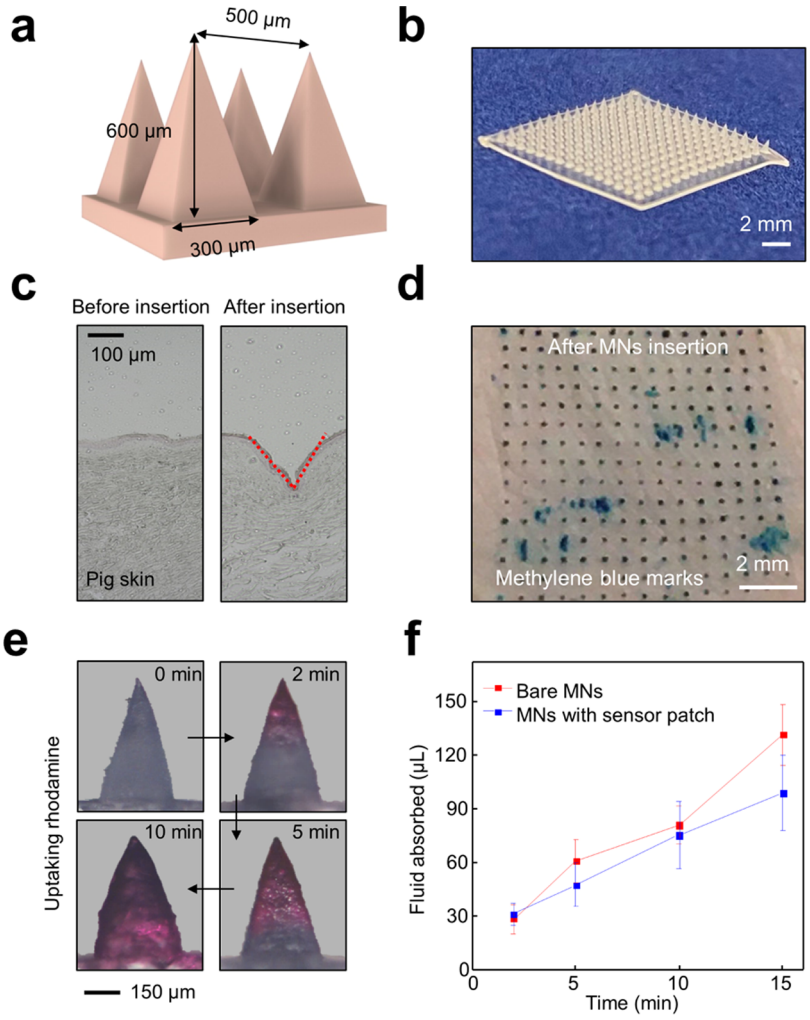


**Figure 3.** Characterization of the hydrogel MNs. (a) Schematic illustration of the hydrogel MNs. (b) Photograph of a 15 × 15 array of the bare MNs. (c) Optical images showcasing pig skin both before and after the insertion of the hydrogel MNs. (d) Image of the pig skin after insertion of hydrogel MN and incubation of methylene blue. (e) Sequential images capturing the hydrogel MNs as they uptake fluid over time. (f) Graph depicting the fluid absorption over time for both the bare MNs (red) and the MNs when integrated with the sensor patch (blue).

strain, consistent with the experimental results. The corresponding optical images and FEA results of the sensor patch without MNs under uniaxial and biaxial stretching are shown in Figure S3a,b, respectively.

**Hydrogel MNs.** Figure 3a presents a schematic of the hydrogel MNs made from MeHA, recognized for its outstanding swelling capacity and mechanical strength, making it favorable for efficient ISF extraction.[41] Specifically, hyaluronic acid with a molecular weight of 250 kDa was selected for synthesizing MeHA, in order to produce a gel that was sufficiently pliable for effective interfacing with both the skin and the sensor, while still maintaining a high enough molecular weight to prevent accelerated degradation rates.[42,43] Figure 3b depicts a 15 × 15 array of these MNs. Figure 3c presents optical images of pig skin both before and after the insertion of the MNs. Despite the abrasions on the porcine skin incurred during preparation for the microneedle insertion study, evidence of the MNs penetrating the pig skin is provided by the methylene blue marks observed in the pores postinsertion.[44,45] This is consistent with the designed length of the MNs exceeding the minimum required for skin penetration and ISF collection (Figure 3d).[22] Figure 3e outlines the results of fluid absorption by the MNs. To simulate the skin, an agarose gel infused with 10 mM Rhodamine B was used, overlaid with a layer of Parafilm M.[39] The samples were initially weighed, then inserted into the agarose gel, and later removed after set time intervals for reweighing and imaging. The presence of the red hue from Rhodamine B, indicative of fluid flow, showcased the extraction and movement of fluid from the MN tips to the sensor patch within 10 min. The volume of the absorbed fluid was calculated based on the difference in weight before and after insertion. Figure 3f indicates a fluid absorption rate of 7.4 ± 0.9 $\mu$L min$^{-1}$ ($R^2$ = 0.970) for bare MNs and 5.3 ± 0.2 $\mu$L min$^{-1}$ ($R^2$ = 0.998) for MNs integrated with the sensor patch. The presence of the sensor patch caused a minor reduction in the fluid absorption rate of the MNs.

**Theoretical Modeling.** In order to calculate the sensing delay through the sensor patch, a modeling schematic and a circuit analogy were employed (Figure 4a). While various approaches exist for ISF extraction and analysis, passive methods stand out, as they avoid extra power consumption and prevent skin inflammation. Our model emphasizes passive methods that rely on diffusive transport for ISF absorption. An inherent time lag is present in these patches between biofluid extraction and sensor responses stemming from the diffusion


https://doi.org/10.1021/acsami.3c12740
ACS Appl. Mater. Interfaces XXXX, XXX, XXX−XXX

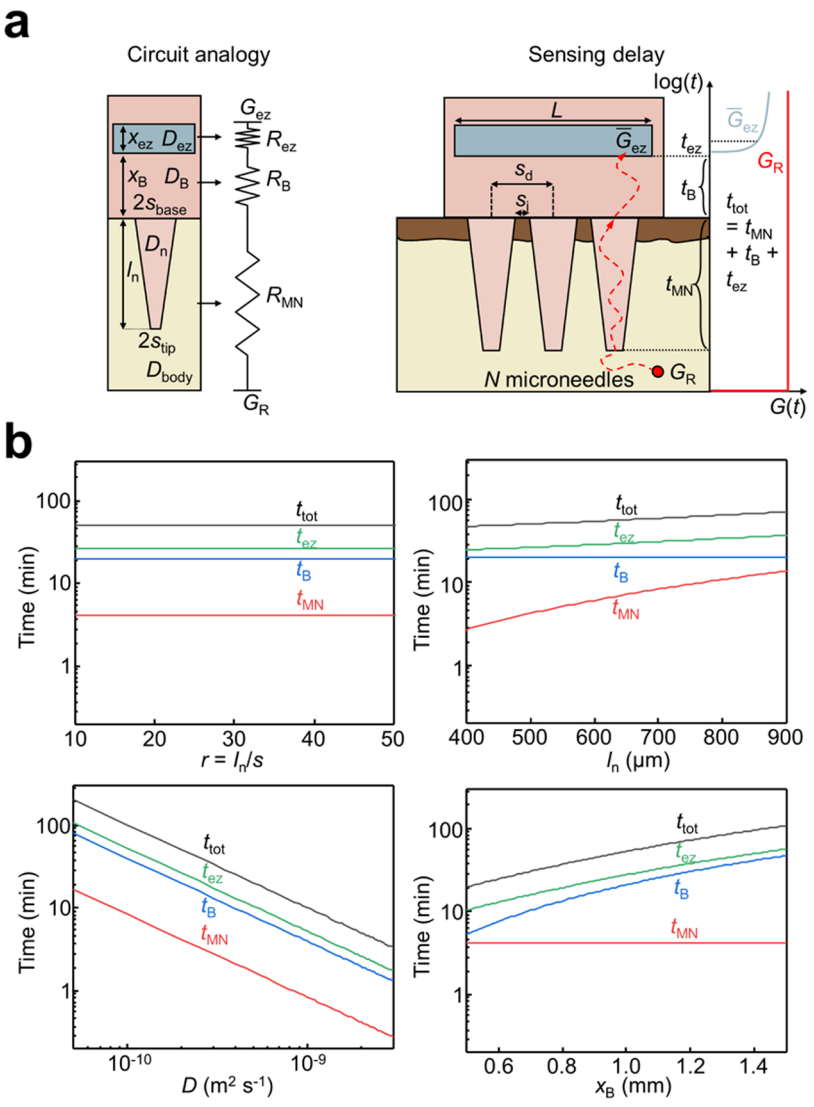


**Figure 4.** Theoretical modeling of the sensing delay. (a) Modeling schematic of the sensor patch with a circuit analogy (left) and the corresponding sensing delay (right). (b) Simulation results of the signal delay in response to the MN aspect ratio ($r = l_n/s$), MN length ($l_n$), diffusivity ($D = D_B = D_{ez} = D_n$), and thickness of the bulk hydrogel patch ($x_B$).

required by analyte molecules to reach the sensor patch's upper end. The delay in sensor response accounted for both the intrinsic transport time between blood and the dermis and the components dependent on the design of the sensor. To model the sensor patch, it was initially regarded as a stack of multiple domains (MN for the hydrogel MN, B for the bulk hydrogel patch, ez for the enzyme layer), with each domain defined by the geometric and physical attributes of the system (diffusivity $D_i$ and thickness $x_i$ for each domain $i$, MN length $l_n$, MN base and tip aperture $s_{base}$ and $s_{tip}$, MN tip-to-tip distance $s_d$, width of the enzyme layer $L$). The MNs were depicted with a blunted shape rather than an idealized conical form to emphasize the significance of the effective tip radius ($s_{tip}$) in modeling. Second, as displayed in the circuit analogy, each domain was modeled with a diffusive resistor ($R_i$ in s m$^{-3}$), in line with the theory of effective media formulation, to approximate the transport of the analyte molecule across the domains.[46] From a phenomenological perspective, the analyte absorption across the MN tip and base is comparable to ion uptake by bacteria,[47] while the transport along the MN length and the bulk hydrogel patch resembles the spreading resistance of a point contact.[48] Lastly, the resistance was multiplied by the corresponding volume of transported biofluid ($V_i$ in m$^3$) to determine the delay time across each domain ($t_i = R_i V_i$). The total response time ($t_{tot}$) equated to the sum of the individual transient contributions necessary for the analyte ($G$) to diffuse across the individual domains until it reached the sensing site (electrode + enzyme)

$$t_{tot} = t_{MN} + t_B + t_{ez} \quad (2)$$

where $t_{MN}$ and $t_B$ are the delays due to the MN and the bulk hydrogel patch, respectively, and $t_{ez}$ is the effective time resulting from diffusion and reaction in the enzyme layer. In other words, any variation of the analyte concentration in the dermis, $G_R$, requires a lag time $t_{tot}$ to be reflected in the upper end of the enzyme layer, where the sensing site is located, $\overline{G}_{ez}(t)$. It is numerically shown that the analyte response within the sensing site requires an initial turn-on delay ($t_{MN} + t_B$) before an exponential-like behavior with time constant equal to $t_{ez}$ reaches the steady state level $\overline{G}_{ez,SS}$.[49]


https://doi.org/10.1021/acsami.3c12740
ACS Appl. Mater. Interfaces XXXX, XXX, XXX−XXX

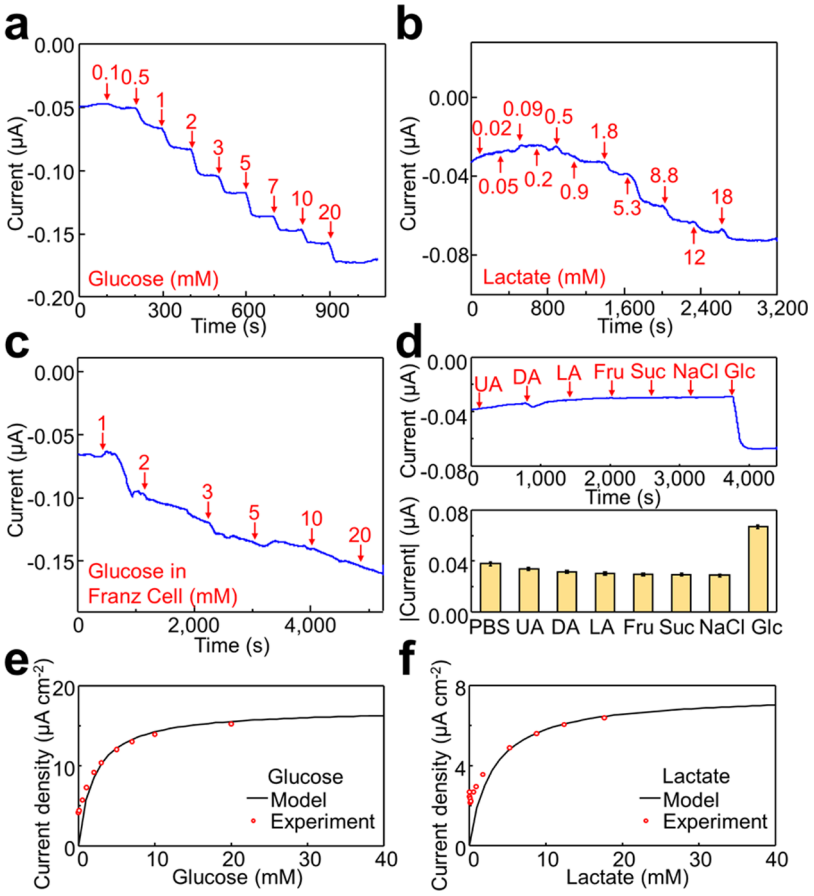


**Figure 5.** Benchtop evaluation. (a, b) Amperometric response of the glucose or lactate sensor patch without MNs in bath solution. (c) Amperometric response of the glucose sensor patch in Franz cell test. (d) Amperometric response (above) and quantification (below) of the glucose sensor patch without MNs against interference species in bath solution. (e, f) Calibration curve of glucose or lactate sensor patch without MNs in bath solution using an MM-inspired equation.

The individual contributions to eq 2 are quantified in terms of geometric and physical modeling of the domain.[49] Specifically

$$t_{MN} = R_{tip}V_{tip,eff} + R_nV_n + R_{base}V_{base,eff} \approx R_nV_n \quad (3)$$

$$t_B = R_BV_B \propto \frac{x_B^2}{D_B} \quad (4)$$

$$t_{ez} = \text{time resulting from enzyme reaction vs molecule supply} \quad (5)$$

In eq 3, $R_{tip} \propto (D_{body}\, s_{tip})^{-1}$, $R_{base} \propto (D_B\, s_{base})^{-1}$, and $R_n \propto l_n (D_n\, s_{tip}^2)^{-2}$ are the resistances of MN tip and base apertures, and MN length, respectively, and $V_{tip,eff}$, $V_{base,eff}$, and $V_n$ are the volumes of transported biofluid corresponding to MN tip and base apertures and to MN volume (truncated pyramid or cone, for example), respectively. In eq 5, $t_{ez}$ results from the balance between the enzymatic conversion of G molecules against its supply from the dermis. For traditional MN-based patches with the enzyme located at the upper end of the patch, the molecule supply is the bottleneck for $t_{ez}$, delaying the overall response time. The analytical results of the signal delay in response to different parameters, including the MN aspect ratio ($r = l_n/s$), the MN length ($l_n$), the diffusivity ($D = D_B = D_{ez} = D_n$), and the thickness of the bulk hydrogel patch ($x_B$), are represented in Figure 4b, respectively. The theory, validated against COMSOL Multiphysics finite element software simulations, confirms that depending on the sensor design the overall delay ranges from several minutes to hundreds of minutes. To justify the experimental characterization, we assumed $s_{base}$ = 150 $\mu$m, $s_{tip}$ = 35 $\mu$m, $s_d$ = 500 $\mu$m, $l_n$ = 600 $\mu$m, $D_{body} = 3 \times 10^{-11}$ m$^2$ s$^{-1}$, and $D_n = D_B = 7.3 \times 10^{-11}$ m$^2$ s$^{-1}$ and apply eq 3.[49] We estimated a diffusion time across the MN equal to $t_{MN,th}$ = 12.7 min, which is consistent with the experimentally measured delay of $t_{MN,exp}$ = 10 min. While this model is tailored to explain MN absorption in a hollow configuration (diffusion through the aperture), the theoretical approach can be adapted for varied extraction across the lateral surface.

**Benchtop Evaluation.** The sensing performance of the sensor patch was initially evaluated and calibrated in a bath solution. For glucose sensing, the glucose sensor patch without MN was connected to the potentiostat and immersed into a 1× phosphate-buffered saline (PBS) solution, with stirring at 200 rpm. Subsequently, the glucose concentration was incrementally elevated from 0 up to 20 mM by adding a 1 M glucose solution. An amperometric method, with onboard reference and counter electrodes applying −0.1 V versus Ag/AgCl, generated the current signal. The glucose concentration was adjusted every 100 s while the current signal stabilized within 60 s (Figure 5a). The calibration curve, demonstrating the current in response to the glucose concentration, is illustrated in Figure S4 and revealed a 0.024 ± 0.002 $\mu$A mM$^{-1}$ ($R^2$ =


https://doi.org/10.1021/acsami.3c12740
ACS Appl. Mater. Interfaces XXXX, XXX, XXX−XXX

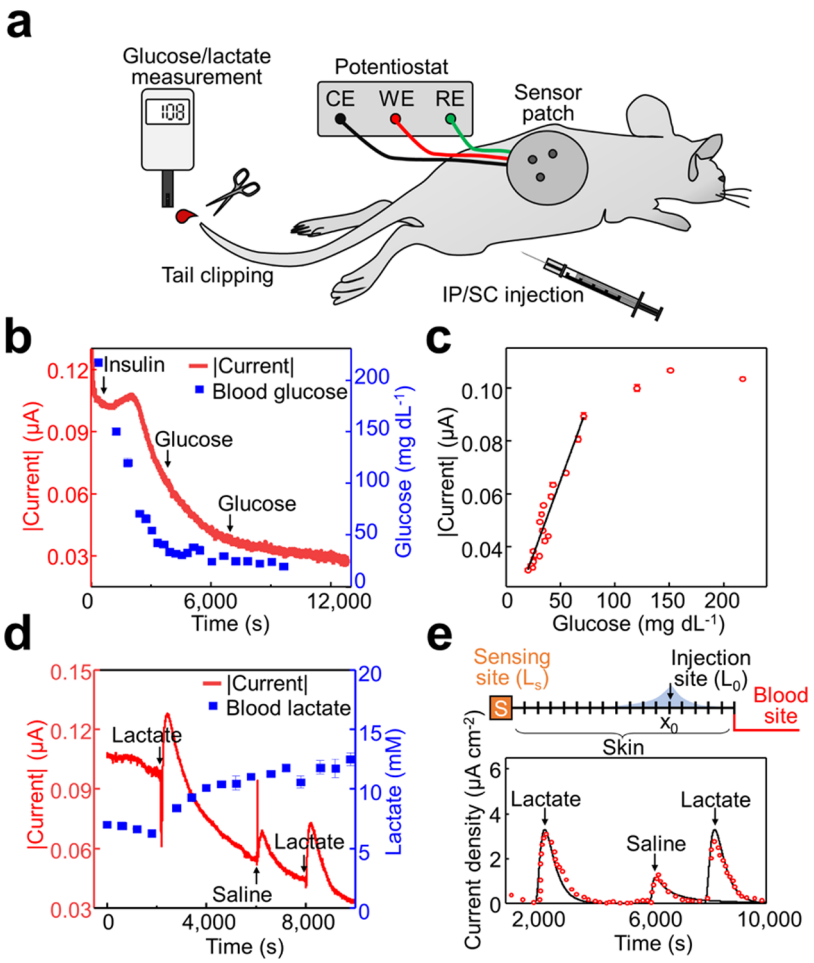


**Figure 6.** In vivo evaluation. (a) Schematic of the in vivo evaluation on mice. (b) Amperometric response of the glucose sensor patch and blood glucose level in the glucose sensing test and (c) the corresponding calibration curve. (d) Amperometric response of the lactate sensor patch and blood lactate level in the lactate sensing test. (e) Schematic of a model for the lactate sensing test (above) and the corresponding calibration curve (below).

0.966) sensitivity within the glucose concentration range of 0.1−3 mM.

The lactate sensing with the lactate sensor patch without MN was performed accordingly, with the only difference being the replacement of 0.2 U $\mu L^{-1}$ GOx with 0.8 U $\mu L^{-1}$ LOx. The amperometric result and calibration curve showed a high sensitivity of 0.68 ± 0.06 $\mu A\ mM^{-1}$ ($R^2$ = 0.950) within the lactate concentration range of 0−1.8 mM, but a saturation point at 1.8 mM was observed (Figure S5a,b). This saturation level of 1.8 mM was insufficient for measuring the normal human lactate level range (1−13 mM). To tackle this issue, an additional drop-casting process of the same glutaraldehyde/bovine serum albumin (BSA) solution, devoid of LOx, was utilized to create a diffusive barrier on top of the enzyme layer of the lactate sensor, leading to a boost in sensor linearity.[50] The amperometric results of the revised lactate sensor are displayed in Figure 5b. The lactate concentration was adjusted after the signal had stabilized, and the current signal stabilized in 120 s. The calibration curve, depicting the current in response to the lactate concentration, is presented in Figure S5c. The lactate sensor had a sensitivity of 0.0030 ± 0.0004 $\mu A\ mM^{-1}$ ($R^2$ = 0.942) and operated within the lactate concentration range of 0.1−12 mM. The sensitivity declined and the current signal at low lactate levels (0−0.1 mM, outside of the normal human lactate range)[51] due to the additional diffusive barrier in lactate transport and sensing.

In order to further examine the combined sensing performance and the MNs' fluid absorption ability, we chose the glucose sensor patch with MNs as the representative for the Franz cell test.[52,53] A schematic of the Franz cell system is represented in Figure S6a. Figure 5c presents the amperometry results of the glucose sensor patch in the Franz cell. The current signal stabilizes within 600 s, and the glucose concentration is adjusted once the signal stabilizes and presents a flat platform within 100 s. Figure S6b exhibits the calibration curve of the current response to the glucose concentration, with a sensitivity of 0.023 ± 0.002 $\mu A\ mM^{-1}$ ($R^2$ = 0.991) within the glucose concentration range of 0−3 mM. As expected, compared to the bath solution, the glucose sensor patch exhibits a longer stabilization time of up to 10 min in the Franz cell due to the signal delay caused by glucose extraction and transport.

We also measured the current signal of the glucose sensor patch without MN in bath solution under fixed glucose concentrations for up to 20 min (1200 s), as illustrated in Figure S7. Following stabilization during the initial 120 s, the current values between 200 and 300 s are averaged as a reference point, and the relative current changes remain below 15% over the 20 min at all glucose levels, demonstrating the


https://doi.org/10.1021/acsami.3c12740
ACS Appl. Mater. Interfaces XXXX, XXX, XXX−XXX

current signal's stability. We also tested the anti-interference performance of the glucose sensor patch without MN in bath solution.[54] We applied amperometry in the presence of common easily oxidized species, such as UA for 0.1 mM uric acid,[55] DA for 0.1 mM dopamine,[56] and LA for 1 mM lactic acid, sugar such as Fru for 1 mM fructose, and Suc for 1 mM sucrose, and electrolyte such as NaCl for 1 mM sodium chloride (NaCl), as depicted in Figure 5d. The absolute current change in response to different species is also illustrated in Figure 5d, showing no significant variation with the addition of interference agents and demonstrating good anti-interference capability.

Additionally, we interpret the results of the electrochemical characterization by calibrating the sensitivity plots for GOx and LOx using a Michaelis−Menten (MM)-inspired equation, as depicted in Figure 5e,f, respectively. To reduce the size effect of the electrodes, we transferred the current signal as the absolute value of the current density. Unlike traditional theory for enzymatic sensors, here many of the assumptions may not hold. In fact, while the traditional theory assumes an initial uniform and homogeneous distribution of molecules, we subsequently introduced the analyte molecules (glucose G or lactate L) at increased concentrations. We reframed the MM formalism's validity for the electrochemical setup that we adopted:

$$J = qN_A t_{ez}\alpha_i \frac{[i]}{K_i + [i]} \tag{6}$$

where $q$ is the electron charge, $N_A$ is the Avogadro number, $t_{ez}$ is the theoretical deposited thickness of the enzyme layer, $[i]$ is the analyte concentration, and $K_i$ is the MM constant. The empirical parameter $\alpha_i$ accounts for deviations from the MM equation's ideal formalism, incorporating (a) the fraction of enzymatic active sites contributing to analyte conversion, (b) the catalytic rate constant efficiency, and (c) the capacitor partition between generated product fluxes.[57−59] The latter process suppresses the efficiency of the overall reaction further; after being generated by the enzyme-analyte complex, only a limited fraction of product molecules approach the sensing site (electrode) to produce an amperometric response, while the remaining amount is lost in the beaker solution. We used eq 6 to calibrate the experimental data. The theory accurately reproduces the experiments, resulting in $K_G$ = 2 mM and $K_L$ = 3 mM, which is consistent with the expected range discussed in the literature.[57,58,60] By using the MM equation for calibration rather than a simple linear fitting, we could extend the sensor patch's effective monitoring range for target biomarkers (glucose or lactate).

**In Vivo Evaluations on Mice.** We assessed the in vivo performance of the sensor patch on mice by comparing it to reference glucose and lactate levels measured from the tail vein using commercial meters and test strips (Figure 6a). The measurements were taken 3 times at 10 min intervals and then averaged to serve as the reference value for comparison to the absolute current signals obtained from the sensor patch by amperometric measurement. Figure S8a displays the image of the sensor patch on the mouse skin immediately upon the insertion of hydrogel MNs and a zoomed-in image of one working electrode on the mouse skin. Figure S8b presents an image of the same area after the sensor patch has been removed following in vivo testing, revealing an array of swollen MNs without signs of detachment, fracture, or degradation. This observation implies that the stability of the system remains uncompromised despite potential alterations to the hydrogel MNs. We also imaged the mouse skin 5 min after MNs removal and confirmed effective insertion by observing an array of pores without any bleeding.

Figure 6b shows the absolute value of the current signal and blood glucose level over time during the glucose sensing test. Due to hyperglycemia in the mouse with a glucose level of 216 mg $dL^{-1}$, insulin was injected intraperitoneally first at 600 s. Subsequently, glucose was injected intraperitoneally at 4000 and 7,000 s. Figure 6c displays a signal delay of 10 min that is obtained through fitting the absolute value of the current signal and the blood glucose level. The sensor patch can measure the glucose level in the range of 20−150 mg $dL^{-1}$ (1.11−8.32 mM), with a sensitivity of 0.00113 ± 0.00008 $\mu$A (mg $dL^{-1}$)$^{-1}$ (or 0.020 ± 0.001 $\mu$A $mM^{-1}$, $R^2$ = 0.917) within the linear range of 20−71 mg $dL^{-1}$ (1.11−3.94 mM). Table S1 contrasts the glucose sensing performance of our device with those of other existing sensors. A strong correlation is evident between the glucose levels detected by our sensor signals and those measured by commercial meters. Furthermore, the signal delay observed in the experiment aligns with both the theoretical prediction and the fluid uptake test conducted earlier.

Figure 6d illustrates the absolute value of the current signal and blood lactate level over time during the lactate sensing test. Lactate was injected subcutaneously twice at 2000 and 8000 s, while only the same amount of PBS solution was injected at 6000 s as a control. The current signal displays a distinctive peak-response pattern that does not correspond to the blood lactate levels. The change in current response for both lactate injections was similar (0.028 ± 0.003 $\mu$A for the first lactate injection, and 0.027 ± 0.002 $\mu$A for the second lactate injection), and significantly higher than the change observed for the PBS injection (0.013 ± 0.002 $\mu$A), indicating the effective response of the sensor patch to lactate. Consistent with the literature that examines the relationship between lactate concentrations in blood and interstitial fluid by varying lactate concentrations through lactate injections,[34] this peak-response pattern may be attributed to lactate's unique metabolic pathway.[61] When lactate is injected subcutaneously, it diffuses into the bloodstream and is then transported to specialized organs, such as the liver, for metabolic processing and utilization.[34] Furthermore, the signal delay (i.e., the time from lactate injection to the peak value of the current signal) was less than 5 min since the sensor patch is closer to the subcutaneously injected lactate, as expected.

To better explain the results of the experiments, we created a physics-based model for the amperometric response to subcutaneously injected lactate. In the model, we represented the situation as a stochastic process with a threshold, as illustrated in Figure 6e. The lactate is injected at a location ($x_0$) that is distant from the sensing site (S, applied sensor patch). On the opposite side of the sensing unit, an absorption site ($x_b$, bloodstream site) is responsible for absorbing the injected molecules. A flow velocity ($u$) is applied to account for the body's response to counteract the lactate injection and enhance its dissipation into the bloodstream.[62] We developed an equation for the time-dependent lactate concentration at the sensing site ($L_s$) by combining balance equations and molecule conservation

$$\frac{\partial L}{\partial t} = D_{body}\frac{\partial^2 L}{(\partial t)^2} - u\frac{\partial L}{\partial x} \tag{7}$$


https://doi.org/10.1021/acsami.3c12740
ACS Appl. Mater. Interfaces XXXX, XXX, XXX−XXX

By applying the boundary conditions ($L(x_0, 0) = L_0\ \delta(x - x_0)$ and $L(x_b, t) = 0$), we quantified the time-dependent concentration on the sensor surface in 3D geometry

$$L_S(t) \propto L_0 \frac{x_0}{\sqrt{6\pi D_{body} t^3}} e^{-(x_0 - ut)^2/6D_{body}t} \quad (8)$$

Therefore, we introduced an empirical factor $\beta$ accounting for the relationship between analyte concentration and amperometric response ($L_S$ to $J$ conversion, and $J$ for absolute value of current density)

$$J_{th} \propto L_S(t) = qN_A\beta \frac{1}{\sqrt{6\pi D_{body} t^3}} e^{-(x_0 - ut)^2/6D_{body}t} \quad (9)$$

The parameter $\beta$ indicates the efficiency of the sensor patch in detecting the particular lactate analyte and is thus linked to the sensor's sensitivity and selectivity.[59]

Figure 6e demonstrates the consistency between the experimental results and the theoretical predictions. To calibrate the response outlined in eq 9, we used the red curve depicted in Figure 6d. Additionally, we eliminated the background noise stemming from drift-affected data by fitting it to an exponential relationship, as shown in Figure S9. Assuming a 2 mm distance ($x_0$ = 2 mm),[63] we fitted the data using parameters outlined in Table S2, based on the noise-free response (red dots in Figure 6g). Despite the intricacy of the in vivo measurement, our theoretical prediction corresponded well with the experimental results.

## CONCLUSIONS

We engineered a stretchable sensor patch that integrates hydrogel MNs. This design aims for swift and minimally invasive extraction of ISF from the skin, while simultaneously providing on-the-spot assessments of biomarker levels. The flexible, serpentine structure of the sensor patch, combined with the adaptive nature of its expandable hydrogel MNs, ensures consistent signal stability by adjustment to skin movements or deformations during the ISF extraction process. This sensing platform merges the functional properties of hydrogel components with advanced electrochemical sensing circuits, thereby securing a stable and reliable sensing process throughout its operation. The efficacy of this integrated approach was substantiated through rigorous in vivo testing, focusing on two pivotal biomarkers: glucose and lactate. In the case of glucose sensing, the sensor demonstrated a remarkable correlation with readings from commercial meters, ensuring its reliability in real-world applications. Moreover, any signal delay encountered during testing was meticulously analyzed by using a comprehensive theoretical model. This detailed analysis not only underscored the platform's robustness but also highlighted potential avenues for further refinement, optimization, and compensation for any delays in signal processing. On the other hand, lactate sensing was subjected to a rigorous theoretical examination through a distinct and specialized metabolic model. Impressively, the predictions generated by this model exhibited close alignment with our hands-on empirical results, echoing insights from previous research in the field. This concurrence opens promising avenues for a more in-depth exploration of lactate levels across a diverse range of physiological compartments. It also provides a foundation for the refinement and improvement of ISF lactate sensors, ensuring their accuracy and reliability in various scenarios. Given the robustness and adaptability of this sensing platform, its potential applications extend beyond the specific biomarkers tested. It lays solid groundwork for the continuous, real-time, in situ monitoring of a plethora of biomarkers in ISF, offering a minimalistic yet effective approach to skin invasiveness. This technological advancement is poised to significantly contribute to the fields of disease management and general health monitoring, driving forward our ability to understand and respond to intricate metabolic changes in real time.

## METHODS

**Fabrication of the Sensor Patch.** A water-soluble PVA solution (10 wt % of Mowiol 4−88 in deionized water) was spin-cast onto a glass slide (Dow Corning) at 2,000 rpm for 30 s and was then annealed at 80 °C for 2 h. Concurrently, the PDMS ink for printing was prepared by mixing base solutions (Sylgard 184 & Dowsil SE 1700, Dow Corning, Inc.) and a curing agent in a weight ratio of 5:5:1. The Ag-TPU ink was created by first dissolving 1.48 g of TPU (Elastollan C60AW) in a combination of 3.76 g of tetrahydrofuran (THF, Sigma-Aldrich, Inc.) and 4 g of dimethylformamide (DMF, Sigma-Aldrich, Inc.), and then blending it with 5.96 g of Ag flakes (average particle size 2−5 $\mu$m, Inframat Advanced Materials, Inc.) using a planetary centrifugal mixer (Thinky, ARE-310). The freshly prepared inks and the Ag/AgCl ink (Cl-4025, Nagase America, Inc.) were directly printed layer-by-layer on the glass slide with a water-soluble PVA layer using an automated nozzle injection system (Nordson EFD) situated on a three-axis computer-controlled translation stage. The resolution was at least 100 $\mu$m in line width, repeatability was ±3 $\mu$m, and the nozzle speed was 2.5 mm $s^{-1}$. The printed layers were then cured at 80 °C for 2 h. Cu wires were connected to the extended pads of the electrodes using Ag paste and baked at 80 °C for 1 h. These junctions were subsequently insulated with PDMS. In the next step, two working electrodes were electroplated with Au (24K Pure Gold Bath Solution, Gold Plating Services, Inc.) using the automotive plating kit (Universal Plater, Chrome Edition, Gold Plating Services, Inc.). A Prussian blue transducer layer was deposited onto the Au-plated Ag-TPU working electrodes by using cyclic voltammetry. The electrolyte solution contained 2.5 mM iron trichloride ($FeCl_3$), 100 mM potassium chloride (KCl), 2.5 mM potassium ferricyanide ($K_3Fe(CN)_6$), and 100 mM hydrochloric acid (HCl). Cyclic voltammetry was conducted from −0.5 to 0.9 V versus Ag/AgCl (3 M NaCl) and reversed 10 times at a rate of 50 mV $s^{-1}$. Following deposition, the sensor electrodes were washed in deionized (DI) water and dried with compressed air. Enzymes were immobilized onto the sensor electrodes by drop-casting a solution of oxidase enzyme (either GOx or LOx), BSA, and the cross-linking agent, glutaraldehyde. The solution for lactate sensors included 0.8 U $\mu L^{-1}$ of LOx, 0.8% BSA, and 0.1% glutaraldehyde. For glucose sensors, the solution contained 0.2 U $\mu L^{-1}$ of GOx, 0.8% BSA, and 0.1% glutaraldehyde. Using a 10 $\mu$L micropipette, 0.5 $\mu$L of solution was placed onto an electrode and then immediately aspirated back off the electrode. This process was repeated three times for each electrode at 1 min intervals. Following drop-casting, the solutions were left to cross-link at room temperature for at least 1 day. Lastly, for lactate sensors, an additional 0.5 $\mu$L of the glutaraldehyde/BSA solution without LOx was drop-cast. The prepared sensor patch was then integrated with hydrogel MNs, as detailed in the next section.

**Integration of MNs into the Sensor Patch.** MeHA was synthesized by mixing 4 g of hyaluronic acid (250 kDa, Creative PEGWorks, Inc.) with 200 mL of DI water, and the solution was stirred at 4 °C overnight. This was followed by the dropwise addition of 133 mL of DMF and 4 mL of methacrylic anhydride (Sigma-Aldrich, Inc.), with pH regulated using 1 M NaOH, while maintaining stirring at 4 °C overnight. Subsequently, NaCl was added to achieve a final concentration of 0.5 M. MeHA was precipitated from the aqueous solution by adding 300 mL of ethanol. The precipitate was


https://doi.org/10.1021/acsami.3c12740
ACS Appl. Mater. Interfaces XXXX, XXX, XXX−XXX

washed three times in ethanol and then subjected to centrifugation for separation. Ultrapure water was utilized to dissolve the precipitate, and this solution was placed in dialysis membranes with a molecular weight cutoff of 12,000 kDa (Sigma-Aldrich, Inc.) and dialyzed against ultrapure water for 7 days, with water changes occurring twice daily. The product was then lyophilized for 3 days to remove all residual water, resulting in purified MeHA. This dried MeHA was stored at −20 °C until needed. For the creation of hydrogel microneedles, the dried MeHA was dissolved in DI water at a concentration of 50 mg $mL^{-1}$. The photoinitiator (2-Hydroxy-4′-(2-hydroxyethoxy)-2-methylpropiophenone) was dissolved in ethanol at a concentration of 100 mg $mL^{-1}$. This photoinitiator solution was added to the hydrogel solution to achieve a final photoinitiator concentration of 0.5 mg $mL^{-1}$ within the hydrogel solution. This solution was subsequently poured into PDMS microneedle molds (Blueacre Technologies, Inc.). The microneedle molds incorporated a 15 × 15 array of square pyramidal microneedles, each with a length of 600 $\mu$m, a base width of 300 $\mu$m, and a tip-to-tip distance of 500 $\mu$m. Following the addition of the hydrogel solution, the microneedle molds underwent centrifugation at 2,500 rpm for 10 min to eliminate bubbles and to facilitate the filling of the hydrogel solution into the tips of the microneedle cavities. The molds were then left at room temperature until the hydrogel was completely dry. Upon drying, the microneedles were extracted from the molds and exposed to UV light of 365 nm for 10 min to induce cross-linking before application. For the assembly of the sensor patch, the sensor, initially fabricated on a PVA-coated glass slide, was submerged in deionized (DI) water overnight to facilitate its release from the glass slide. Simultaneously, to prepare the hydrogel substrate, we created a hydrogel solution consisting of 50 mg $mL^{-1}$ MeHA and 0.5 mg $mL^{-1}$ photoinitiator in DI water. This solution was then poured into a PDMS mold to form a thin, flat substrate and left to dry thoroughly. Upon drying, the substrate was detached from the mold, and the sensor was transferred onto it. The MN mold was subsequently prepared, into which the hydrogel solution was added, and centrifuged. The sensor patch, placed on the flat hydrogel substrate, was then introduced into the MN mold and left to dry completely. Following drying, the integrated sensor patch, now combined with the hydrogel MNs, was extracted from the mold. Any excess hydrogel was carefully trimmed off, and the patch was cross-linked using 365 nm UV radiation for 10 min before application.

**Mechanical Tests.** Standard tensile tests were conducted to determine the elastic moduli of the sensor patch without MNs, hydrogel MNs, and the sensor patch (devices with MNs). The specimens were loaded on the chuck of a tensile testing machine (ESM303, Mark-10) and then stretched at an elongation rate of 5% per minute. For the measurement of the relative resistance change ($\Delta R/R$), one working electrode was selected as the representative, and the electrode and its extended pad were connected to a source meter (Keithley 2400; Keysight, Inc.) via a conducting Cu wire during cyclic stretching up to 1000 times at the applied strain of 10, 15, and 20% with the elongation rate of 100% per minute, respectively. $\Delta R$ is the difference between current resistance and initial resistance, and $R$ is the initial resistance value.

**Fluid Uptake and Swelling Tests.** Fluid uptake was tested on the hydrogel MNs and sensor patches. A skin model was made with 1.4% agarose (Fisher Scientific, Inc.) combined with 10 mM Rhodamine B (Sigma-Aldrich, Inc.) and covered with a layer of Parafilm M. The MNs were pierced through the Parafilm M layer with a spring-loaded application tool (Micropoint, Inc.) and swelled for 2, 5, 10, or 15 min. Samples were fixed by a top holder (75 g) to prevent detachment. Samples were weighed before and after swelling to evaluate fluid uptake, and microscope images were taken to evaluate swelling and visualize Rhodamine B uptake into the MNs. Swelling ratio tests were performed on the sensor patches similarly, and the perimeter ($P$) of the hydrogel MN array was measured every 5 min until saturation. The swelling ratio was defined as $\Delta P/P$, where $\Delta P$ is the difference between current perimeter and initial perimeter, and $P$ is the initial perimeter value.

**Mechanical Simulation.** A commercial software package, Abaqus, was used for FEA to investigate the strain levels impacting the conductive layers of the sensor patch under conditions of stretching and swelling deformation. Three layers of the sensor patch on a PDMS film were modeled to enable the analysis of uniaxial and biaxial stretching. The tie-constraint option was utilized to bond each interface between the layers and the PDMS film. The mechanical properties of PDMS were defined using the Neo-Hookean hyperelastic model based on uniaxial tension test results and a Poisson's ratio of 0.495. Both Ag-TPU and the hydrogel were treated as linear elastic materials with a modulus of 0.248 MPa and a Poisson's ratio of 0.4. For stretching, displacement boundary conditions were implemented on the side surfaces of the PDMS film, while out-of-plane displacement was constrained on the surface opposing the sensor patch. For the analysis of swelling-like deformation, the hydrogel was selected as the host region using the embedded region constraint option, being considered a linear elastic material with a modulus of 16.7 MPa and a Poisson's ratio of 0.46. To roughly estimate the strain concentration on the conductive layer resulting from the swelling of the hydrogel encasing the sensor patch, a thermal expansion simulation was performed, driven by the conceptual similarity. The top and bottom surfaces of the hydrogel were restrained by rigid surfaces, leaving the square region designated for MN fabrication exposed. The maximum principal strains inflicted on the conductive layer were plotted, corresponding to the point at which the swelling ratio of the FEA result matched the value observed experimentally.

**Ex Vivo Pig Skin Studies and Histology.** Pig skin was procured from the lower belly of a 2-year-old specimen. The skin was sanitized with ethanol and shaved to eliminate any excess hair. The hydrogel MN patches were then positioned on the excised skin and inserted by using a spring-loaded application tool. Subsequent to this application, methylene blue (1 mg $mL^{-1}$, Sigma-Aldrich, Inc.) was applied to the skin and allowed to incubate for 1 min. Afterward, the skin was cleansed and imaged to view the insertion of the MNs. Following this, the skin samples were preserved in a formalin solution for 3 days, which was succeeded by histological processing that included staining with hematoxylin and eosin.

**Simulation of Signal Delay in Response to Different Parameters.** A unit cell was defined, which included two rectangular domains (the sensor patch and skin dermis) interconnected by a hollow parallelepiped with a square cross section (representing an individual hydrogel MN). The sensing site was positioned at the upper end of the sensor patch. The simulation was conducted by using COMSOL Multiphysics finite element software. Initially, the physical laws within each domain were defined, followed by the application of flux continuity across the interfaces. The diffusion of the analyte was governed by Fick's second law, with corresponding diffusion coefficient $D_i$ in each domain. The enzyme layer was implicated in enzymatic conversion (from analyte G to product P) under the assumption of oxygen availability. Given the following chemical reaction, the balance equation in the enzyme layer was defined as

$$E + G \underset{}{\overset{k_f, k_r}{\longleftrightarrow}} EG \overset{k_c}{\rightarrow} E + P \tag{10}$$

where $E$, EG, and $P$ are the free enzyme, intermediate complex, and product molecules, respectively, and $k_f$, $k_r$, and $k_c$ are the rate constants for the forward, reverse, and catalytic steps of the conversion process, respectively. Finally, the redox reaction on the electrode surface was described by the Butler−Volmer formalism.

**Benchtop Evaluations in Bath Solution.** Glucose or lactate sensor patches, without MNs, were fabricated on a glass slide and connected to the potentiostat. These were then immersed in a 1× PBS solution and stirred at 200 rpm. Following this, the concentration of the target biomarker was incrementally increased (for glucose: 0, 0.1, 0.5, 1, 2, 3, 5, 7, 10, 20 mM; for lactate: 0, 0.02, 0.05, 0.09, 0.2, 0.5, 0.9, 1.8, 5.3, 8.8, 12, and 18 mM) by adding the concentrated solution (either 1 M glucose solution or 100 mM lactate solution). An amperometric method, employing onboard reference and counter electrodes, was used to generate the current signal by applying −0.1 V


https://doi.org/10.1021/acsami.3c12740
ACS Appl. Mater. Interfaces XXXX, XXX, XXX−XXX

versus Ag/AgCl. The sensing performance was displayed using smoothed lines, and calibration was determined based on the raw results. The final 50 s of the stabilized data were recorded as means ± SD for the current response at each biomarker concentration.

**Benchtop Evaluations in Franz Cell.** To mimic skin insertion, the glucose sensor patch was fabricated and penetrated through one layer of Parafilm M with its hydrogel MNs, exposing it to a 1× PBS solution. To prevent potential detachment due to swelling, we secured the glucose sensor patch with a top holder. The glucose concentration in the PBS solution was then altered (0, 1, 2, 3, 5, 10, and 20 mM) by injecting a concentrated glucose solution through the side sampling port. The current signal was generated by employing an amperometric method with onboard reference and counter electrodes applying −0.1 V versus Ag/AgCl. The sensing performance was showcased with smoothed lines, and calibration was calculated based on raw results. The last 100 s of the stabilized data were recorded as means ± SD for the current response at each biomarker concentration.

**Long-Term Stability and Anti-Interference Tests.** For the long-term stability test, a glucose sensor patch without MNs was fabricated on the glass slide and connected to the potentiostat. It was then submerged in a 1× PBS solution and stirred at 200 rpm. Following this, the glucose concentration was adjusted to specific values (0, 0.1, 0.5, 1, 2, 3, 5, 7, 10, and 20 mM) by adding a 1 M glucose solution. An amperometric method, using onboard reference and counter electrodes applying −0.1 V versus Ag/AgCl, generated the current signal for more than 1200 s. The sensing performance was represented by using smoothed lines. The stabilized current data at 200−300 s were averaged as the reference current response $I_{ref}$, while the relative current change was calculated by

$$I_{rel} = (I_t - I_{ref})/I_{ref} \quad (11)$$

where $I_t$ is the current response at certain time $t$ and $I_{ref}$ is the reference current response by averaging the stabilized current data at 200−300 s. For the anti-interference test, a glucose sensor patch without MNs was fabricated on the glass slide and connected to the potentiostat. It was then submerged in a 1× PBS solution and stirred at 200 rpm. Subsequently, interference species, including 0.1 mM uric acid, 0.1 mM dopamine, 1 mM lactic acid, 1 mM fructose, 1 mM sucrose, and 1 mM NaCl, were added at 10 min intervals, with 1 mM glucose added at the end. An amperometric method, using onboard reference and counter electrodes applying −0.1 V vs Ag/AgCl, generated the current signal. The sensing performance was represented using smoothed lines with calculations based on raw results. The absolute value of the final 100 s of the stabilized data was recorded as mean ± SD for the absolute current response to each species.

**In Vivo Evaluations on Mice.** All animal experimental procedures were reviewed and approved by the Purdue Animal Care and Use Committee (PACUC) under protocol number 2001001998. Male NU/J athymic nude mice were procured from Jackson Laboratory (Bar Harbor, ME,), with each mouse receiving one sensor patch at each experimental time point. All animals were maintained in a 12 h light/dark cycle, with humidity and temperature kept constant. The animals were anesthetized using isoflurane vapor (5.0% for induction, 1.5−3.0% for maintenance) mixed with oxygen (flow rate: 500 mL $min^{-1}$ for induction, 30−70 mL $min^{-1}$ for maintenance), regulated by an automated system (SomnoSuite, Kent Scientific Corporation, Inc.). After initial induction, the animal was positioned in left lateral recumbency for anesthesia maintenance, allowing the sensor patch to be attached to the right lateral side of the dorsal skin, while the abdomen remained accessible for intraperitoneal injections. The animal's temperature was kept at 35.9−37.5 °C by using a heat pad. The sensor patch was attached to the right lateral dorsal skin and was ensured to puncture the skin using a spring-loaded application tool and gentle pinching with the index finger and thumb. It was then secured in place with Tegaderm tape (3 M Tegaderm transparent film dressing). An incision was made to the tail tip using sterile surgical scissors (501739, World Precision Instruments, Inc.), and the tail was gently massaged to draw blood from the tail vein to measure blood glucose or lactate levels using a commercially available glucometer (Accu-Chek Guide Me, Roche Diabetes Care, Inc.) or a lactate meter (Lactate Plus, Nova Biomedical, Inc.). Simultaneously, the sensor patch was connected to the potentiostat, and an amperometric method with onboard reference and counter electrodes applying −0.1 V vs Ag/AgCl was used for measurement. For the glucose measurement experiment, we injected 2 U $kg^{-1}$ (~80 g $kg^{-1}$) insulin in 200 μL of PBS and 1 g $kg^{-1}$ glucose in 200 μL of PBS intraperitoneally. For the lactate measurement experiment, we injected 1 g $kg^{-1}$ lactate in 200 μL of PBS subcutaneously and PBS (as control) subcutaneously directly underneath the site of the inserted sensory microneedle patch. Blood glucose or lactate levels were measured three times approximately every 10 min, and averaged to serve as the reference value. The sensing performance was presented with smoothed lines, and calculations were performed based on raw results. For blood glucose levels measured at one specific point in time, the absolute values of current data for the subsequent 100 s were recorded as means ± SD for the current response. The set of data points was fitted with different signal delays to achieve the best-fitting results.

## ■ ASSOCIATED CONTENT

### Supporting Information

The Supporting Information is available free of charge at https://pubs.acs.org/doi/10.1021/acsami.3c12740.

Images of the sensor patch and hydrogel MNs (Figure S1); mechanical characterization and simulation of the sensor patch (Figures S2 and S3); benchtop evaluations (Figures S4−S7); images of in vivo evaluations (Figure S8); comparison of glucose sensing performance (Table S1); fitting of the amperometric response of the lactate sensor patch during the lactate sensing test (Figure S9) (Table S2) (PDF)

## ■ AUTHOR INFORMATION


### Corresponding Authors

**Muhammad A. Alam** − *Elmore Family School of Electrical and Computer Engineering, Purdue University, West Lafayette, Indiana 47907, United States;* orcid.org/0000-0001-8775-6043; Email: alam@purdue.edu

**Jacqueline C. Linnes** − *Weldon School of Biomedical Engineering and Department of Public Health, Purdue University, West Lafayette, Indiana 47907, United States;* orcid.org/0000-0003-4962-0908; Email: jlinnes@purdue.edu

**Hyowon Lee** − *Weldon School of Biomedical Engineering and Center for Implantable Devices, Purdue University, West Lafayette, Indiana 47907, United States;* orcid.org/0000-0001-7628-1441; Email: hwlee@purdue.edu

**Chi Hwan Lee** − *School of Materials Engineering, Purdue University, West Lafayette, Indiana 47907, United States; Weldon School of Biomedical Engineering, School of Mechanical Engineering, and Center for Implantable Devices, Purdue University, West Lafayette, Indiana 47907, United States;* orcid.org/0000-0002-4868-7054; Email: lee2270@purdue.edu

### Authors

**Yumin Dai** − *School of Materials Engineering, Purdue University, West Lafayette, Indiana 47907, United States;* orcid.org/0000-0003-3141-9384

**James Nolan** − *Weldon School of Biomedical Engineering, Purdue University, West Lafayette, Indiana 47907, United States;* orcid.org/0000-0003-0008-8009




https://doi.org/10.1021/acsami.3c12740
ACS Appl. Mater. Interfaces XXXX, XXX, XXX−XXX

**Emilee Madsen** − *Weldon School of Biomedical Engineering, Purdue University, West Lafayette, Indiana 47907, United States;* orcid.org/0000-0002-8175-6592
**Marco Fratus** − *Elmore Family School of Electrical and Computer Engineering, Purdue University, West Lafayette, Indiana 47907, United States;* orcid.org/0000-0002-2131-6843
**Junsang Lee** − *Weldon School of Biomedical Engineering, Purdue University, West Lafayette, Indiana 47907, United States*
**Jinyuan Zhang** − *Weldon School of Biomedical Engineering, Purdue University, West Lafayette, Indiana 47907, United States;* orcid.org/0009-0005-5890-2976
**Jongcheon Lim** − *Weldon School of Biomedical Engineering, Purdue University, West Lafayette, Indiana 47907, United States*
**Seokkyoon Hong** − *Weldon School of Biomedical Engineering, Purdue University, West Lafayette, Indiana 47907, United States;* orcid.org/0009-0007-6540-0389

Complete contact information is available at: https://pubs.acs.org/10.1021/acsami.3c12740

## Author Contributions

[▽]Y.D., J.N., E.M., and M.F. contributed equally to this work. M.A.A., J.C.L., H.L., and C.H.L. conceived the concept, planned the project, and supervised the research. Y.D., J.N., E.M., J.Z., J.C.L., H.L., and C.H.L. designed, fabricated, characterized, and implemented the wearable sensor patch. E.M. and J.C.L. fabricated and characterized the hydrogel microneedles. J.L. and C.H.L. designed and conducted the mechanical simulation. M.F. and M.A.A. designed and conducted the simulation of the sensing performance. J.L. and H.L. designed and conducted the in vivo test on mice. Y.D., J.N., E.M., M.F., J.L., J.Z., J.L., and C.H.L. wrote the manuscript. All authors commented on the paper.

## Funding

This work was funded by Eli Lilly and Company (Grant Number: 40003523). C.H.L. acknowledges the Leslie A. Geddes Endowment at Purdue University.

## Notes

The authors declare no competing financial interest.

## REFERENCES

(1) Sempionatto, J. R.; Lasalde-Ramírez, J. A.; Mahato, K.; Wang, J.; Gao, W. Wearable Chemical Sensors for Biomarker Discovery in the Omics Era. *Nat. Rev. Chem.* **2022**, *6*, 899−915.
(2) Zhao, J.; Guo, H.; Li, J.; Bandodkar, A. J.; Rogers, J. A. Body-Interfaced Chemical Sensors for Noninvasive Monitoring and Analysis of Biofluids. *Trends Chem.* **2019**, *1*, 559−571.
(3) Tehrani, F.; Teymourian, H.; Wuerstle, B.; Kavner, J.; Patel, R.; Furmidge, A.; Aghavali, R.; Hosseini-Toudeshki, H.; Brown, C.; Zhang, F.; Mahato, K.; Li, Z.; Barfidokht, A.; Yin, L.; Warren, P.; Huang, N.; Patel, Z.; Mercier, P. P.; Wang, J. An Integrated Wearable Microneedle Array for the Continuous Monitoring of Multiple Biomarkers in Interstitial Fluid. *Nat. Biomed. Eng.* **2022**, *6*, 1214−1224.
(4) Lee, H.; Hong, Y. J.; Baik, S.; Hyeon, T.; Kim, D.-H. Enzyme-Based Glucose Sensor: From Invasive to Wearable Device. *Adv. Healthcare Mater.* **2018**, *7*, No. 1701150.
(5) Samant, P. P.; Niedzwiecki, M. M.; Raviele, N.; Tran, V.; Mena-Lapaix, J.; Walker, D. I.; Felner, E. I.; Jones, D. P.; Miller, G. W.; Prausnitz, M. R. Sampling Interstitial Fluid from Human Skin Using a Microneedle Patch. *Sci. Transl. Med.* **2020**, *12*, No. eaaw0285.
(6) Tran, B. Q.; Miller, P. R.; Taylor, R. M.; Boyd, G.; Mach, P. M.; Rosenzweig, C. N.; Baca, J. T.; Polsky, R.; Glaros, T. Proteomic Characterization of Dermal Interstitial Fluid Extracted Using a Novel Microneedle-Assisted Technique. *J. Proteome Res.* **2018**, *17*, 479−485.
(7) Sim, D.; Brothers, M. C.; Slocik, J. M.; Islam, A. E.; Maruyama, B.; Grigsby, C. C.; Naik, R. R.; Kim, S. S. Biomarkers and Detection Platforms for Human Health and Performance Monitoring: A Review. *Adv. Sci.* **2022**, *9*, No. 2104426.
(8) Miller, P. R.; Taylor, R. M.; Tran, B. Q.; Boyd, G.; Glaros, T.; Chavez, V. H.; Krishnakumar, R.; Sinha, A.; Poorey, K.; Williams, K. P.; Branda, S. S.; Baca, J. T.; Polsky, R. Extraction and Biomolecular Analysis of Dermal Interstitial Fluid Collected with Hollow Microneedles. *Commun. Biol.* **2018**, *1*, No. 173.
(9) Min, J.; Tu, J.; Xu, C.; Lukas, H.; Shin, S.; Yang, Y.; Solomon, S. A.; Mukasa, D.; Gao, W. Skin-Interfaced Wearable Sweat Sensors for Precision Medicine. *Chem. Rev.* **2023**, *123*, 5049−5138.
(10) Kim, J.; Campbell, A. S.; de Avila, B. E.; Wang, J. Wearable Biosensors for Healthcare Monitoring. *Nat. Biotechnol.* **2019**, *37*, 389−406.
(11) Saifullah, K. M.; Faraji Rad, Z. Sampling Dermal Interstitial Fluid Using Microneedles: A Review of Recent Developments in Sampling Methods and Microneedle-Based Biosensors. *Adv. Mater. Interfaces* **2023**, *10*, No. 2201763.
(12) Kim, J.; Sempionatto, J. R.; Imani, S.; Hartel, M. C.; Barfidokht, A.; Tang, G.; Campbell, A. S.; Mercier, P. P.; Wang, J. Simultaneous Monitoring of Sweat and Interstitial Fluid Using a Single Wearable Biosensor Platform. *Adv. Sci.* **2018**, *5*, No. 1800880.
(13) Pu, Z.; Zou, C.; Wang, R.; Lai, X.; Yu, H.; Xu, K.; Li, D. A Continuous Glucose Monitoring Device by Graphene Modified Electrochemical Sensor in Microfluidic System. *Biomicrofluidics* **2016**, *10*, No. 011910.
(14) Kim, J.; Campbell, A. S.; Wang, J. Wearable Non-Invasive Epidermal Glucose Sensors: A Review. *Talanta* **2018**, *177*, 163−170.
(15) Alam, M. A.; Saha, A.; Fratus, M. Reliable Sensing with Unreliable Sensors: Rethinking the Theoretical Foundation of Field-Deployed Wearable/Implantable/Environmental Sensors. *Innov. Emerg. Technol.* **2022**, *09*, No. 2240003.
(16) Zheng, M.; Wang, Z.; Chang, H.; Wang, L.; Chew, S. W. T.; Lio, D. C. S.; Cui, M.; Liu, L.; Tee, B. C. K.; Xu, C. Osmosis-Powered Hydrogel Microneedles for Microliters of Skin Interstitial Fluid Extraction within Minutes. *Adv. Healthcare Mater.* **2020**, *9*, No. e1901683.
(17) Turner, J. G.; White, L. R.; Estrela, P.; Leese, H. S. Hydrogel-Forming Microneedles: Current Advancements and Future Trends. *Macromol. Biosci.* **2020**, *21*, No. 2000307.
(18) Han, J. H.; Kim, C. R.; Min, C. H.; Kim, M. J.; Kim, S.-N.; Ji, H. B.; Yoon, S. B.; Lee, C.; Choy, Y. B. Microneedles Coated with Composites of Phenylboronic Acid-Containing Polymer and Carbon Nanotubes for Glucose Measurements in Interstitial Fluids. *Biosens. Bioelectron.* **2023**, *238*, No. 115571.
(19) Caliò, A.; Dardano, P.; Di Palma, V.; Bevilacqua, M. F.; Di Matteo, A.; Iuele, H.; De Stefano, L. Polymeric microneedles based enzymatic electrodes for electrochemical biosensing of glucose and lactic acid. *Sens. Actuators B: Chem.* **2016**, *236*, 343−349.
(20) Dardano, P.; Rea, I.; De Stefano, L. Microneedles-based electrochemical sensors: New tools for advanced biosensing. *Curr. Opin. Electrochem.* **2019**, *17*, 121−127.
(21) Freeman, D. M. E.; Cass, A. E. G. A Perspective on Microneedle Sensor Arrays for Continuous Monitoring of the Body's Chemistry. *Appl. Phys. Lett.* **2022**, *121*, No. 070502.
(22) Kashaninejad, N.; Munaz, A.; Moghadas, H.; Yadav, S.; Umer, M.; Nguyen, N.-T. Microneedle Arrays for Sampling and Sensing Skin Interstitial Fluid. *Chemosensors* **2021**, *9*, No. 83.
(23) Larrañeta, E.; Lutton, R. E. M.; Woolfson, A. D.; Donnelly, R. F. Microneedle Arrays as Transdermal and Intradermal Drug Delivery Systems: Materials Science, Manufacture and Commercial Development. *Mater. Sci. Eng. R Rep.* **2016**, *104*, 1−32.
(24) Zhang, J.; Zheng, Y.; Lee, J.; Hoover, A.; King, S. A.; Chen, L.; Zhao, J.; Lin, Q.; Yu, C.; Zhu, L.; Wu, X. Continuous Glucose

Monitoring Enabled by Fluorescent Nanodiamond Boronic Hydrogel. *Adv. Sci.* **2023**, *10*, No. 2203943.
(25) Zheng, H.; GhavamiNejad, A.; GhavamiNejad, P.; Samarikhalaj, M.; Giacca, A.; Poudineh, M. Hydrogel Microneedle-Assisted Assay Integrating Aptamer Probes and Fluorescence Detection for Reagentless Biomarker Quantification. *ACS Sens.* **2022**, *7*, 2387−2399.
(26) Xu, N.; Zhang, M.; Xu, W.; Ling, G.; Yu, J.; Zhang, P. Swellable PVA/PVP Hydrogel Microneedle Patches for the Extraction of Interstitial Skin Fluid toward Minimally Invasive Monitoring of Blood Glucose Level. *Analyst* **2022**, *147*, 1478−1491.
(27) Oh, N. G.; Hwang, S. Y.; Na, Y. H. Fabrication of a PVA-Based Hydrogel Microneedle Patch. *ACS Omega* **2022**, *7*, 25179−25185.
(28) Luo, Y.; Abidian, M. R.; Ahn, J.-H.; Akinwande, D.; Andrews, A. M.; Antonietti, M.; Bao, Z.; Berggren, M.; Berkey, C. A.; Bettinger, C. J.; Chen, J.; Chen, P.; Cheng, W.; Cheng, X.; Choi, S.-J.; Chortos, A.; Dagdeviren, C.; Dauskardt, R. H.; Di, C.-a.; Dickey, M. D.; et al. Technology Roadmap for Flexible Sensors. *ACS Nano* **2023**, *17*, 5211−5295.
(29) He, R.; Niu, Y.; Li, Z.; Li, A.; Yang, H.; Xu, F.; Li, F. A Hydrogel Microneedle Patch for Point-of-Care Testing Based on Skin Interstitial Fluid. *Adv. Healthcare Mater.* **2020**, *9*, No. 1901201.
(30) Li, J.; Lu, H.; Wang, Y.; Yang, S.; Zhang, Y.; Wei, W.; Qiao, Y.; Dai, W.; Ge, R.; Dong, H. Interstitial Fluid Biomarkers' Minimally Invasive Monitoring Using Microneedle Sensor Arrays. *Anal. Chem.* **2022**, *94*, 968−974.
(31) Chang, H.; Zheng, M.; Yu, X.; Than, A.; Seeni, R. Z.; Kang, R.; Tian, J.; Khanh, D. P.; Liu, L.; Chen, P.; Xu, C. A Swellable Microneedle Patch to Rapidly Extract Skin Interstitial Fluid for Timely Metabolic Analysis. *Adv. Mater.* **2017**, *29*, No. 1702243.
(32) Parrilla, M.; Detamornrat, U.; Domínguez-Robles, J.; Donnelly, R. F.; De Wael, K. Wearable Hollow Microneedle Sensing Patches for the Transdermal Electrochemical Monitoring of Glucose. *Talanta* **2022**, *249*, No. 123695.
(33) Dervisevic, M.; Alba, M.; Yan, L.; Senel, M.; Gengenbach, T. R.; Prieto-Simon, B.; Voelcker, N. H. Transdermal Electrochemical Monitoring of Glucose via High-Density Silicon Microneedle Array Patch. *Adv. Funct. Mater.* **2021**, *32*, No. 2009850.
(34) Spehar-Délèze, A.-M.; Anastasova, S.; Vadgama, P. Monitoring of Lactate in Interstitial Fluid, Saliva and Sweat by Electrochemical Biosensor: The Uncertainties of Biological Interpretation. *Chemosensors* **2021**, *9*, No. 195.
(35) Kim, K. B.; Choi, H.; Jung, H. J.; Oh, Y.-J.; Cho, C.-H.; Min, J. H.; Yoon, S.; Kim, J.; Cho, S. J.; Cha, H. J. Mussel-Inspired Enzyme Immobilization and Dual Real-Time Compensation Algorithms for Durable and Accurate Continuous Glucose Monitoring. *Biosens. Bioelectron.* **2019**, *143*, No. 111622.
(36) Ribet, F.; Stemme, G.; Roxhed, N. Real-Time Intradermal Continuous Glucose Monitoring Using a Minimally Invasive Microneedle-Based System. *Biomed. Microdevices* **2018**, *20*, No. 101.
(37) Horwood, C. Chapter Eleven - Ionic Liquids as Electrolytes for Electrochemistry. In *Ionic Liquids in Analytical Chemistry*; Carda-Broch, S.; Ruiz-Angel, M., Eds.; Elsevier, 2022; pp 329−342.
(38) Sim, K.; Li, Y.; Song, J.; Yu, C. Biaxially Stretchable Ultrathin Si Enabled by Serpentine Structures on Prestrained Elastomers. *Adv. Mater. Technol.* **2019**, *4*, No. 1800489.
(39) Ziesmer, J.; Tajpara, P.; Hempel, N. J.; Ehrström, M.; Melican, K.; Eidsmo, L.; Sotiriou, G. A. Vancomycin-Loaded Microneedle Arrays against Methicillin-Resistant Staphylococcus Aureus Skin Infections. *Adv. Mater. Technol.* **2021**, *6*, No. 2001307.
(40) Zhang, K.; Feng, W.; Jin, C. Protocol Efficiently Measuring the Swelling Rate of Hydrogels. *MethodsX* **2020**, *7*, No. 100779.
(41) Chang, H.; Zheng, M.; Yu, X.; Than, A.; Seeni, R. Z.; Kang, R.; Tian, J.; Khanh, D. P.; Liu, L.; Chen, P.; Xu, C. A Swellable Microneedle Patch to Rapidly Extract Skin Interstitial Fluid for Timely Metabolic Analysis. *Adv. Mater.* **2017**, *29*, No. 1702243.
(42) Luo, T.; Tan, B.; Zhu, L.; Wang, Y.; Liao, J. A Review on the Design of Hydrogels with Different Stiffness and Their Effects on Tissue Repair. *Front. Bioeng. Biotechnol.* **2022**, *10*, No. 817391.
(43) Ren, Y.; Zhang, H.; Wang, Y.; Du, B.; Yang, J.; Liu, L.; Zhang, Q. Hyaluronic Acid Hydrogel with Adjustable Stiffness for Mesenchymal Stem Cell 3D Culture via Related Molecular Mechanisms to Maintain Stemness and Induce Cartilage Differentiation. *ACS Appl. Bio. Mater.* **2021**, *4*, 2601−2613.
(44) Moronkeji, K.; Todd, S.; Dawidowska, I.; Barrett, S. D.; Akhtar, R. The Role of Subcutaneous Tissue Stiffness on Microneedle Performance in a Representative In Vitro Model of Skin. *J. Controlled Release* **2017**, *265*, 102−112.
(45) Cheung, K.; Han, T.; Das, D. B. Effect of Force of Microneedle Insertion on the Permeability of Insulin in Skin. *J. Diabetes Sci. Technol.* **2014**, *8*, 444−452.
(46) Fratus, M.; Alam, M. A. Universal Scaling Theory of Electrochemical Immunosensors: An Analytical Approach to Define and Compare Performance Metrics. *Appl. Phys. Lett.* **2023**, *122*, No. 054102.
(47) Berg, H. C. *Random Walks in Biology: New and Expanded Edition*; Princeton University Press, 2018.
(48) Karmalkar, S.; Mohan, P. V.; Nair, H. P.; Yeluri, R. Compact Models of Spreading Resistances for Electrical/Thermal Design of Devices and ICs. *IEEE Trans. Electron Devices* **2007**, *54*, 1734−1743.
(49) Fratus, M.; Lim, J.; Nolan, J. K.; Madsen, E.; Dai, Y.; Lee, C. H.; Linnes, J. C.; Lee, H.; Alam, M. A.; Alam, A. Geometry-Defined Response Time and Sensitivity for Microneedle-Based Amperometric Sensors. *IEEE Sens. J.* **2023**, *23*, 14285−14294.
(50) Riccardi, C.; McCormick, S.; Kasi, R.; Kumar, C. A Modular Approach for Interlocking Enzymes in Whatman Paper. *Angew. Chem., Int. Ed.* **2018**, *57*, 10158−10162.
(51) De la Paz, E.; Saha, T.; Del Caño, R.; Seker, S.; Kshirsagar, N.; Wang, J. Non-Invasive Monitoring of Interstitial Fluid Lactate through an Epidermal Iontophoretic Device. *Talanta* **2023**, *254*, No. 124122.
(52) Pulsoni, I.; Lubda, M.; Aiello, M.; Fedi, A.; Marzagalli, M.; von Hagen, J.; Scaglione, S. Comparison Between Franz Diffusion Cell and a novel Micro-physiological System for In Vitro Penetration Assay Using Different Skin Models. *SLAS Technol.* **2022**, *27*, 161−171.
(53) Larrañeta, E.; Stewart, S.; Fallows, S. J.; Birkhäuer, L. L.; McCrudden, M. T. C.; Woolfson, A. D.; Donnelly, R. F. A Facile System to Evaluate In Vitro Drug Release from Dissolving Microneedle Arrays. *Int. J. Pharm.* **2016**, *497*, 62−69.
(54) Zheng, M.; Zhang, Y.; Hu, T.; Xu, C. A Skin Patch Integrating Swellable Microneedles and Electrochemical Test Strips for Glucose and Alcohol Measurement in Skin Interstitial Fluid. *Bioeng. Transl. Med.* **2022**, No. e10413.
(55) Desideri, G.; Castaldo, G.; Lombardi, A.; Mussap, M.; Testa, A.; Pontremoli, R.; Punzi, L.; Borghi, C. Is it Time to Revise the Normal Range of Serum Uric Acid Levels? *Eur. Rev. Med. Pharmacol. Sci.* **2014**, *18*, 1295−1306.
(56) Liu, X.; Liu, J. Biosensors and Sensors for Dopamine Detection. *View* **2020**, *2*, No. 20200102.
(57) Jin, X.; Bandodkar, A. J.; Fratus, M.; Asadpour, R.; Rogers, J. A.; Alam, M. A. Modeling, Design Guidelines, and Detection Limits of Self-Powered Enzymatic Biofuel Cell-Based Sensors. *Biosens. Bioelectron.* **2020**, *168*, No. 112493.
(58) Jin, X.; Fisher, T. S.; Alam, M. A. Generalized Compact Modeling of Nanoparticle-Based Amperometric Glucose Biosensors. *IEEE Trans. Electron Devices* **2016**, *63*, 4924−4932.
(59) Rasitanon, N.; Ittisoponpisan, S.; Kaewpradub, K.; Jeerapan, I. Wearable Electrodes for Lactate: Applications in Enzyme-Based Sensors and Energy Biodevices. *Anal. Sens.* **2023**, *3*, No. e202200066.
(60) Jin, X.; Alam, M. A. Generalized Modeling Framework of Metal Oxide-Based Non-Enzymatic Glucose Sensors: Concepts, Methods, and Challenges. *IEEE Trans. Biomed. Eng.* **2020**, *67*, 679−687.
(61) Valenza, F.; Pizzocri, M.; Salice, V.; Chevallard, G.; Fossali, T.; Coppola, S.; Froio, S.; Polli, F.; Gatti, S.; Fortunato, F.; Comi, G. P.; Gattinoni, L. Sodium Bicarbonate Treatment during Transient or Sustained Lactic Acidemia in Normoxic and Normotensive Rats. *PLoS One* **2012**, *7*, No. e46035.


https://doi.org/10.1021/acsami.3c12740
*ACS Appl. Mater. Interfaces* XXXX, XXX, XXX−XXX

(62) Alam, M. *ECE 695A Reliability Physics of Nanotransistors*, 2013. https://nanohub.org/resources/16560 ( accessed 2023−08−12).
(63) Xie, Y.; Shao, R.; Lin, Y.; Wang, C.; Tan, Y.; Xie, W.; Sun, S. Improved Therapeutic Efficiency against Obesity through Transdermal Drug Delivery Using Microneedle Arrays. *Pharmaceutics* **2021**, *13*, No. 827.


https://doi.org/10.1021/acsami.3c12740
*ACS Appl. Mater. Interfaces* XXXX, XXX, XXX−XXX